https://doi.org/10.1016/j.ijhydene.2020.09.216

Atomistic simulation of the effect of the dissolution and adsorption of hydrogen atoms on the fracture of α-Fe single crystal under tensile load

Zheng Wang[a], Xiaoming Shi[a], Xu-Sheng Yang[b,d], Wangqiang He[a], San-Qiang Shi[c**], Xingqiao Ma[a*]

a. Department of physics, University of Science and Technology Beijing, Beijing, China
b. Advanced Manufacturing Technology Research Centre, Department of Industrial and Systems Engineering, The Hong Kong Polytechnic University, Hung Hom, Kowloon, Hong Kong, China
c. Department of Mechanical Engineering, The Hong Kong Polytechnic University, Hung Hom, Kowloon, Hong Kong, China
d. Hong Kong Polytechnic University Shenzhen Research Institute, Shenzhen 518057, China

Abstract

The local hydrogen distribution has significant influences on hydrogen embrittlement. In this work, mode-I fractures of (010)[100] pre-cracked α-Fe single crystal containing dissolved and absorbed hydrogen atoms are simulated by molecular dynamics and the time-stamped force-bias Monte Carlo methods. Statistics show that when located near the {112} plane, hydrogen atoms accelerate cleavage fracture and suppress the slip of {112}<111>; when located on the {110} plane, they promote martensite transformation and increase {110}<111> slip. Most adsorbed hydrogen atoms are concentrated near the inside of the crack surface and suppress fracture early by stress relaxation; therein concentrates stresses inside the matrix, and causes microvoid-coalescence fracture.

Highlights

The hydrogen distribution and crack growth are linked by statistics.

Hydrogen promotes fracture by inhibiting {112}<111> slip in α-Fe.

The hydrogen on the {110} planes can enhance the martensitic transformation.

* Corresponding author. Department of physics, University of Science and Technology Beijing, Beijing, China
Email Address: xqma@sas.ustb.edu.cn (Xingqiao Ma)
** Corresponding author. Department of Mechanical Engineering, The Hong Kong Polytechnic University, Hung Hom, Kowloon, Hong Kong, China
Email Address: san.qiang.shi@polyu.edu.hk (Sanqiang Shi)

Adsorption of hydrogen can promote microvoid-coalescence fracture.

The voids in the matrix can be caused by hydrogen near the crack surface.

Keywords

Hydrogen embrittlement; Statistics of hydrogen distribution; Martensitic transformation; α-Fe single crystal; Atomistic simulation

1. Introduction

Hydrogen embrittlement (HE), first reported in 1874 [1], is an accelerated fracture phenomenon caused by the introduction of hydrogen during the manufacturing or service process [2–7]. It may be caused by aggregated hydrogen molecules [8] or brittle hydrides [9–12], or occur suddenly under a low load with very low hydrogen concentration (C_H) after a long delay. The latter leads to catastrophic failures in iron, steel, and other structural materials [13–16], especially in service conditions such as the production, storage and transportation of oil, natural gas and hydrogen [17–19]. Due to the complexity of the materials and the difficulty in detecting local hydrogen distribution [3–5,7,20–26], further exploration is necessary.

In previous research [5,20,26,27], the hydrogen-enhanced decohesion (HEDE) mechanism for HE was proposed. Several studies in support of this view have been made [23,28–31] but require very high C_H [32–34]. However, in iron and ferroalloys, more phenomena led by hydrogen have been observed, such as: softening or hardening [30,32,35,36], different fracture morphologies and shear-slips [21,33,35,37], void nucleation [33], and concomitant martensitic transformations (MTs) during HE [3,4,18,38–42]. Such research findings highlight the importance of hydrogen transport, distribution, and influence on plasticity, and have spawned the hydrogen-enhanced local plasticity (HELP) mechanism [4,11,21,43,44]. Although no direct reason for HE has been provided, HELP indicates that hydrogen can promote dislocation emission, multiplication, and motion; therein accumulates hydrogen atoms in the active slip system, and resulting in the localization and planarity of the shear slip by migrating

dislocations and suppressing the cross slips.

Since HE can be caused by both the internally dissolved and environmentally adsorbed hydrogen atoms, Lynch proposed the adsorption-induced dislocation emission (AIDE) mechanism [6,7]. With AIDE, hydrogen atoms will diffuse to the internal crack tip caused by stress, or be adsorbed to the external crack tip from the environment. These atoms enhance dislocation emission within a few nanometers of the crack tip and are quickly taken away by these dislocations. Due to stresses in this process, crack propagation and void nucleation can be promoted. Strain, adsorption, and movement of hydrogen atoms significantly affect each other and fracture [45]. Nagumo noticed the interaction of strain, hydrogen, and vacancies, and proposed the hydrogen-enhanced strain-induced vacancies (HESIV) mechanism [3,37]. According to this theory, the combination of hydrogen atoms and vacancies in the plastic zone reduces their mobility and stabilizes these vacancies, thereby localizing strain and forming clusters. This is considered to be the origin of microvoids and can also reduce the stress-bearing capacity. AIDE attempts to provide a unified image of HE, and HESIV has also been observed in some studies [46,47]. However, hydrogen atoms sites in different places have different diffusivities [48], and the positions where hydrogen affects HE most are still under debate [29,30,34,49–51], making previous findings inconclusive.

As previously reported, hydrogen distribution highly affected the HE susceptibility in steel [19,48]. To some extent, it determines HE, so molecular dynamics (MD) and other atomistic simulation methods are widely used to obtain clearer images [24,25,29,47,51–54]. However, most studies are conducted at high C_H and high loading rates, which might affect the migration and distribution of hydrogen. In this work, we statistically discuss the effect of hydrogen atom positions on HE, using MD simulation of mode-I fracture of α-Fe single crystal under low C_H; thereafter, HE caused by adsorbed hydrogen atoms is studied combining with MD and the time-stamped force-bias Monte Carlo (tfMC) method [55], for improving time scale.

2. Simulation Methods

2.1 MD simulation of the models with dissolved hydrogen atoms

The C_H of the α-Fe single crystal models with dissolved hydrogen atoms was 0.04% (7.14 wppm), 0.06% (10.7 wppm), 0.07% (12.5 wppm), and 0.08% (14.3 wppm). The projection onto the (001) plane for each of the models is shown in Fig. 1(a). With a lattice constant of 2.8664Å for stacked unit cells, we generated structures with a size of 31.2nm (W) × 31.59nm(L) × 3.6nm(B), with each containing about 300,000 atoms. Periodic boundary conditions were available in the [001] direction, while in [100] and [010] directions, the vacuum layer (in a thickness of 8Å) was applied outside of the simulation region. As shown in Fig. 1(b), hydrogen atoms were randomly distributed in the tetrahedral interstitials (Tet-sites) with a uniform distribution by the Knuth-shuffle algorithm [56]. Then, a (010)[100] oriented semi-elliptical pre-crack was generated, with a length of 10.8nm (marked as a) and an opening of 0.86 nm (marked as b). Using the Lammps simulator [57] and MD method, the simulation was carried out under temperature T = 300 K and time step size t_s = 0.1 fs. We relaxed the models for 15 ps in an isothermal-isobaric ensemble (NPT) [58,59], and then gradually loaded them along the [010] direction with a rate of 3.1×10^{8} s^{-1}. Each time, both the ends (marked as c) were clamped after adding about 2‰ of the stretch and then run for 15 ps in a canonical ensemble (NVT) [58]. For each model, the total simulation lasted 450ps, and the stress intensity factor was calculated by tracking the crack [60]. The Fe-Fe interaction was described by the embedded atom method (EAM) potential [61], and the Fe-H interaction was fitted by Ramasubramaniam et al. [62].

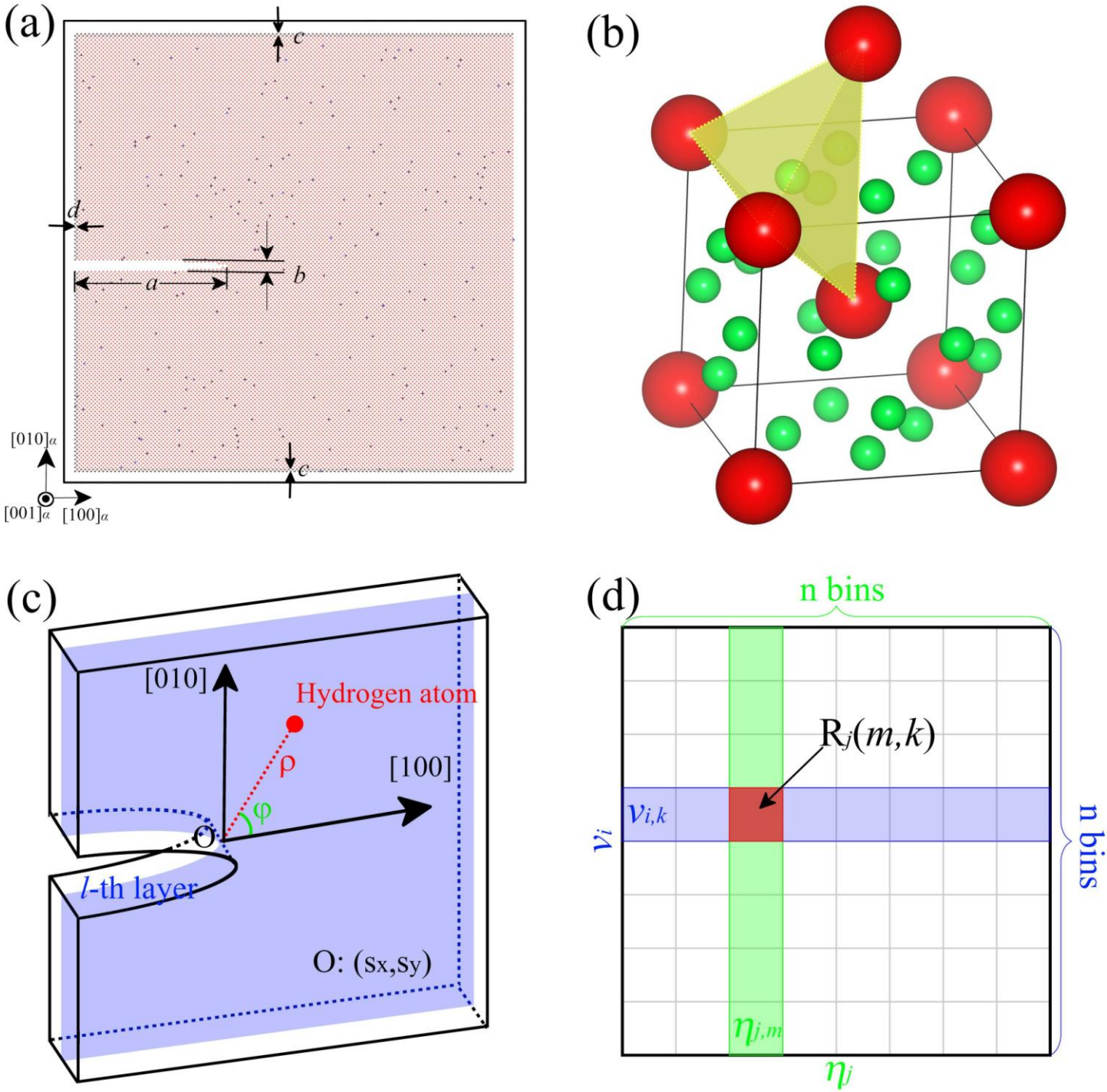

Fig. 1 Sample of the specimen model. (a) Initial structure with hydrogen atoms randomly distributed in the Tet-sites. (b) Tet-sites in α-Fe. (c) Coordinates of hydrogen atoms with the origin set at the crack tip. (d) The piecewise linearity of η_j and v_i correlation functions.

In this work, the atomic stress is calculated by[63]：

$$\sigma_a = \frac{1}{\Omega_a}\left(m_a \otimes v_a + \frac{1}{2}\sum_{b\neq a} r_{a,b} \otimes f_{a,b}\right) \#(1)$$

where Ω_a is the Voronoi volume of an atom, calculated using voro++[64], m_a, v_a are the atom's mass and velocity, respectively, and $r_{a,b}$, and $f_{a,b}$ are the relative position vector and the force between atoms, respectively.

The stress intensity factor $K_{I,tip}(t)$ for mode-I fracture at moment t is extrapolated by its definition[65–67]:

$$\begin{gathered} K_I(r,t) = \sqrt{2\pi r}\,\sigma_{yy}(r,\theta=0,t) \\ K_{I,tip}(t) = \lim_{r\to 0} K_I(r,t) \end{gathered} \#(2)$$

Then the critical value K_{IC} is:

$$K_{IC} = \max\left[K_{I,tip}(t)\right] \#(3)$$

Since the fracture strength can only be expressed by the value of the crack tip, we denote $K_{I,tip}$ as K_I below. To determine whether hydrogen promotes fracture, the crack growth rate was studied. Assuming that the coordinates of the crack tip at time t are $(S_x(C_H,t),S_y(C_H,t))$, where x and y represent the [100]α and [010]α directions, respectively, the instantaneous velocity v_i of the crack is:

$$v_i(C_H,t) = \frac{d\,S_x\,(C_H,t)}{d\,t} \#(4)$$

From the moment t_r, sampling in the window with a width of t_w = 10 ps, the average value is:

$$v_w(C_H,t_r) = \frac{1}{t_w}\int_{t_r}^{t_r+t_w} v_i(C_H,t)dt \#(5)$$

It is assumed that hydrogen atoms affect the fracture independently of each other. As shown in Fig. 1(c), the position of the hydrogen atom on the (001)α plane can be expressed as η(ρ, φ). Let:

$$\eta_1 = \rho \#(6)$$

$$\eta_2 = \begin{cases} \varphi, \varphi < 90^\circ \\ 180^\circ - \varphi, \varphi \geq 90^\circ \end{cases} \#(7)$$

Then, η_j(j=1,2) and v_i can be associated to reflect the effects of hydrogen on the fracture.

As shown in Fig. 1(d), in order to satisfy the linear condition, η_j and v_i are divided into

n groups. Marking the sets with the m-th η_j and the k-th v_i as $\eta_{j,m}$ and $v_{i,k,}$ respectively, we can then use the Pearson coefficient R_j (m, k) to express the correlation. Setting n=50 and satisfying H_m and V_k:

$$\left\{H_m \in \eta_{j,m} | \frac{mA}{n} \le H_m - \min(\eta_j) \le \frac{(m+1)A}{n}\right\}, m = 1,2,3,\cdots,n$$
$$\left\{V_k \in v_{i,k} | \frac{kB}{n} \le V_k - \min(v_i) \le \frac{(k+1)B}{n}\right\}, k = 1,2,3,\cdots,n \quad \#(8)$$
$$A = \max(\eta_j) - \min(\eta_j)$$
$$B = \max(v_i) - \min(v_i)$$

R_j(m,k) can be defined as below [68,69] :

$$R_j(m,k) = \frac{\sum(H_m - \bar{H}_m)(V_k - \bar{V}_k)}{\sqrt{\sum(H_m - \bar{H}_m)^2 \sum(V_k - \bar{V}_k)^2}} \#(9)$$

We only accept R_j when $p \le 0.05$, where p is [68]:

$$P_j(m,k) = \int_0^{1-R_j^2(m,k)} \frac{t^{\frac{1}{2}f-1}}{(1-t)^{\frac{1}{2}}} dt \Big/ \int_0^1 \frac{t^{\frac{1}{2}f-1}}{(1-t)^{\frac{1}{2}}} dt \ \#(10)$$

and f is the degrees of freedom.

In this work, the numerical libraries Shapely [70], Numpy [71], and Scipy [68] were used for post-processing. Fig. 1(b) was drawn using the data visualization software VESTA [72]. Using the data analysis software Ovito [73], the dislocations [74] and the nearby phases [75] within 50Å of the crack tip were identified, and respectively, the blue, green, red, and white colors were used to represent the α, γ, ε phases and the disordered structure in snapshots in this paper. Using the built-in local-weighted regression (LWR) algorithm [76], the statistical library statsmodels [77] was used to analyze the effect of hydrogen on phase transitions.

2.2 MD+tfMC simulation with hydrogen adsorption

The initial model of pure iron and the boundary conditions shown in Fig. 2(a) are set to be similar to those of Fig. 1(a). The model was firstly relaxed for 150,000 steps in the NVT ensemble, T = 300 K, t_s =1 fs, and then loaded 30 times. Under each load, the model was stretched by about 2.5‰, and the MD and the tfMC were performed for 15,000 steps, respectively. The maximum displacement Δd of an atom for tfMC

was:

$$\Delta d = \frac{\sqrt{3}}{2} p a_{Fe} \#(11)$$

where p = 0.1, a_{Fe} = 2.8664 Å.

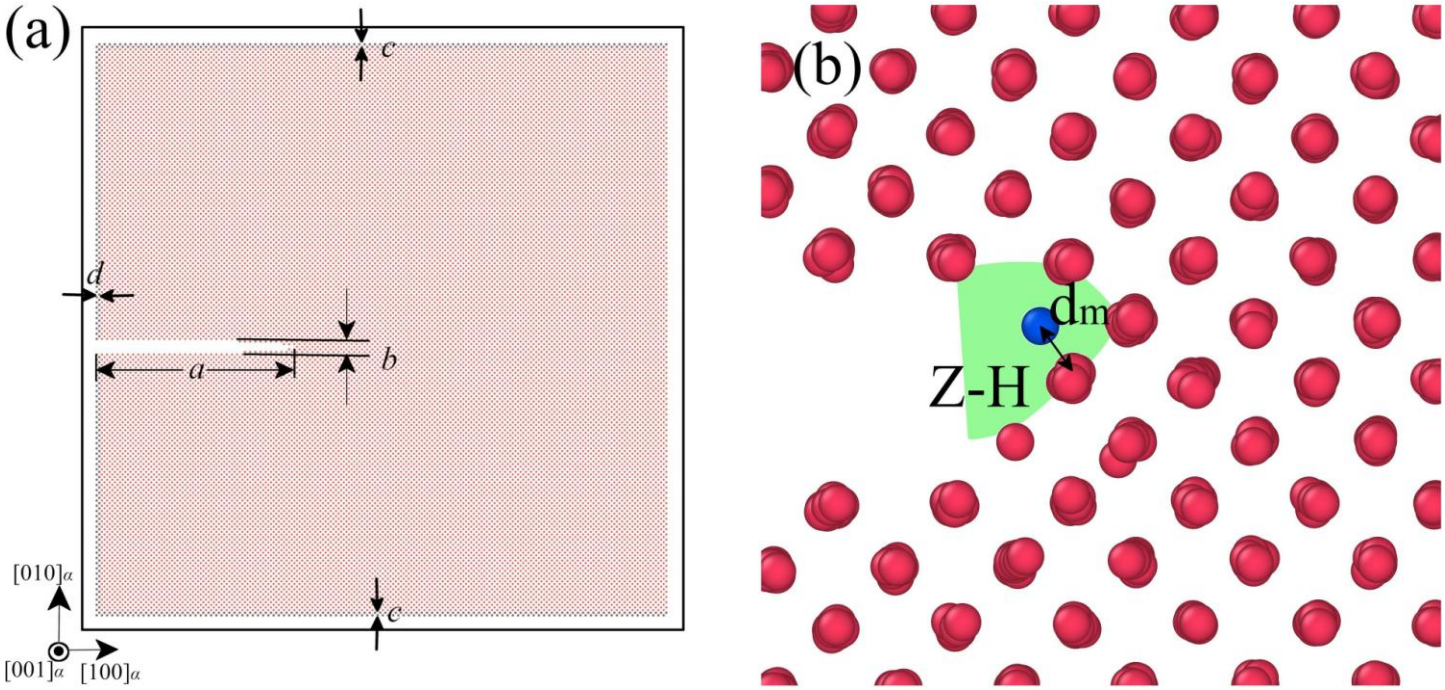

Fig. 2 The model with adsorbed hydrogen atoms. (a) Initial model, pure Iron. (b) Zone Z-H for hydrogen insertion. The distance between the newly inserted hydrogen atom and its nearest Fe atom should be larger than d_m.

The MD+tfMC model for hydrogen adsorption is basically the same as the pure iron model. As shown in Fig. 2(b), these hydrogen atoms (colored as deep blue) were newly inserted into the zone Z-H (colored as green) step by step and restricted to d_m to their nearest iron neighbors.

We set t_s = 0.5 fs and then relaxed the model for 30,000 steps in the NVT ensemble. Assuming that the hydrogen atom was at the Tet-site, Δd was:

$$\Delta d = \frac{\sqrt{5}}{4} p a_{Fe} \#(12)$$

Subsequently, we ran 15000 steps in tfMC.

Then, tensions were applied n = 45 times, each time with a strain rate of d_ε = 2.5‰. We define the $C_H(t)$ after inserting hydrogen atoms in the t-th tension as:

$$C_H(t) = \frac{N_H(t)}{N_H(t) + N_{Fe}} \#(13)$$

$N_H(t)$ and N_{Fe} are the number of hydrogen and iron atoms at moment t, thus:

$$N_H(t) = \frac{C_H(t)}{1 - C_H(t)} N_{Fe} \#(14)$$

$$F_C = \frac{N_{HF}}{N_{HF} + N_{Fe}} \#(15)$$

And the final hydrogen atoms N_{HF} is:

$$N_{HF} = \frac{F_C}{1 - F_C} N_{Fe} \#(16)$$

In this work, $F_C \sim 0.7‰$ (12.5 wppm) was chosen as the final hydrogen concentration.

The hydrogen adsorption capacity should be increased since the interstitial sites enlarge with the model's volume. Suppose the number of insertable atoms is proportional to the volume; considering the boundary conditions, we obtain:

$$\Delta C_H(t) \propto 1 + \delta_l \cdot t \#(17)$$

where $\delta_l = 2.5‰$.

Let:

$$\Delta C_H(t) = (1 + \delta_l \cdot t) f \#(18)$$

In which f is a scale factor. Due to the extremely low C_H in α-Fe, we can write C_H after the i-th tension as:

$$\begin{aligned} C_H(i) &= \sum_{t=0}^{i} \Delta C_H(t) \\ &= f + \sum_{t=1}^{i} (1 + \delta_l t) f \\ &= (i+1) f + \sum_{t=1}^{i} \delta_l f \\ &= (i+1)\left(1 + \frac{i}{2}\delta_l\right) f \end{aligned} \#(19)$$

With the total number of tensions n, we obtain:

$$f = \frac{F_C}{(n+1)\left(1 + \frac{n}{2}\delta_l\right)} \#(20)$$

Substitute Eq. (20) into Eq. (18), we have:

$$\Delta C_H(t) = \frac{(1 + \delta_l t)}{(n+1)\left(1 + \frac{n}{2}\delta_l\right)} F_C \#(21)$$

Then the number of hydrogen atoms that should be inserted in the t-th tension can be

written as:

$$\begin{aligned}\Delta N_H(t) &= \Delta C_H(t) \cdot \left(N_{Fe} + N_H(t)\right) \\ &= (1+\delta_l t) f \cdot \left(1 + \frac{C_H(t)}{1 - C_H(t)}\right) N_{Fe} \\ &= \frac{(1+\delta_l t) F_C}{\left(1 - C_H(t)\right)(n+1)\left(1 + \frac{\delta_l n}{2}\right)} N_{Fe}\end{aligned} \quad \#(22)$$

The density functional theory (DFT) results show that in an equilibrated α-Fe lattice [54], the distance between hydrogen atoms is $d_{HH} \geq 2.1$Å; thus, we choose t_{HH} = 0.75 ps as the minimum interval of hydrogen insertion to ensure sufficient movement. Since tfMC can improve the time scale, but the interval of each step is inequality [55], each tension's process was divided into two stages. The first stage included 30 sections, each of which comprises two parts. In the latter stage, a 15000-step tfMC simulation was performed after tension. The first part of the previous stage was a tfMC calculation for 5000 steps if there were adsorbed hydrogen atoms, and the second part contained ten cycles. Each cycle included a hydrogen insertion process and 100 steps of full MD relaxation. Before confirming whether to accept a new randomly insertion, the number of inserted hydrogen atoms ΔN and the interval Δt to the last insertion were detected to ensure that $\Delta N < \Delta N_H(t)$ and $\Delta t > \Delta t_{HH}$. Hydrogen atoms were randomly distributed along the [001] direction, and then tfMC calculation was performed on these atoms.

We use the partial pair-coefficient function (PCF) to check the distance between two hydrogen atoms [78]:

$$g(r) = \frac{1}{\rho_H N_H} \left\langle \sum_{i \neq j} \delta\left(r - \left|\boldsymbol{R}_i - \boldsymbol{R}_j\right|\right) \right\rangle \#(23)$$

where ρ_H and N_H are the average atomic density and the number of hydrogen atoms respectively, and $\mathbf{R}_i$, $\mathbf{R}_j$ are the position vectors.

The averaged atomic stresses σ in different zones are used for stress analyzing. According to the definition of stress invariants[79]:

$$I_1 = \sigma_{xx} + \sigma_{yy} + \sigma_{zz}$$
$$I_2 = \begin{vmatrix} \sigma_{yy} & \tau_{yz} \\ \tau_{zy} & \sigma_{zz} \end{vmatrix} + \begin{vmatrix} \sigma_{zz} & \tau_{zx} \\ \tau_{xz} & \sigma_{xx} \end{vmatrix} + \begin{vmatrix} \sigma_{xx} & \tau_{xy} \\ \tau_{yx} & \sigma_{yy} \end{vmatrix} \#(24)$$
$$I_3 = \begin{vmatrix} \sigma_{xx} & \tau_{xy} & \tau_{xz} \\ \tau_{yx} & \sigma_{yy} & \tau_{yz} \\ \tau_{zx} & \tau_{zy} & \sigma_{zz} \end{vmatrix}$$

the maximum principal stress σ_{max} and the maximum shear stress τ_{max} are calculated by:

$$\sigma^3 - I_1\sigma^2 + I_2\sigma - I_3 = 0$$
$$\sigma_{max} = \max(\sigma) \quad \#(25)$$
$$\tau_{max} = \frac{1}{2}(\max(\sigma) - \min(\sigma))$$

3. Results and discussion

3.1 The influences of dissolved hydrogen atoms on mode-I fractures of α-Fe single crystal

3.1.1 Crack propagation

Fig. 3(a,b) shows Sx and K_I, with the pure iron data from our previous work [60]. HE occurs only with C_H = 0.07%, and the unstable crack propagation starting from 194 ps, is 36 ps earlier than that of pure iron. Later, K_I remained at lower values, and the crack length (L_c) was longer. However, all K_{IC}s listed in Tab. 1 with $C_H > 0$ were obtained earlier than C_H = 0 and had lower values, which indicates that the dependence on the continuously decreasing K_{IC} promotes fracture, and implies the importance of hydrogen distribution.

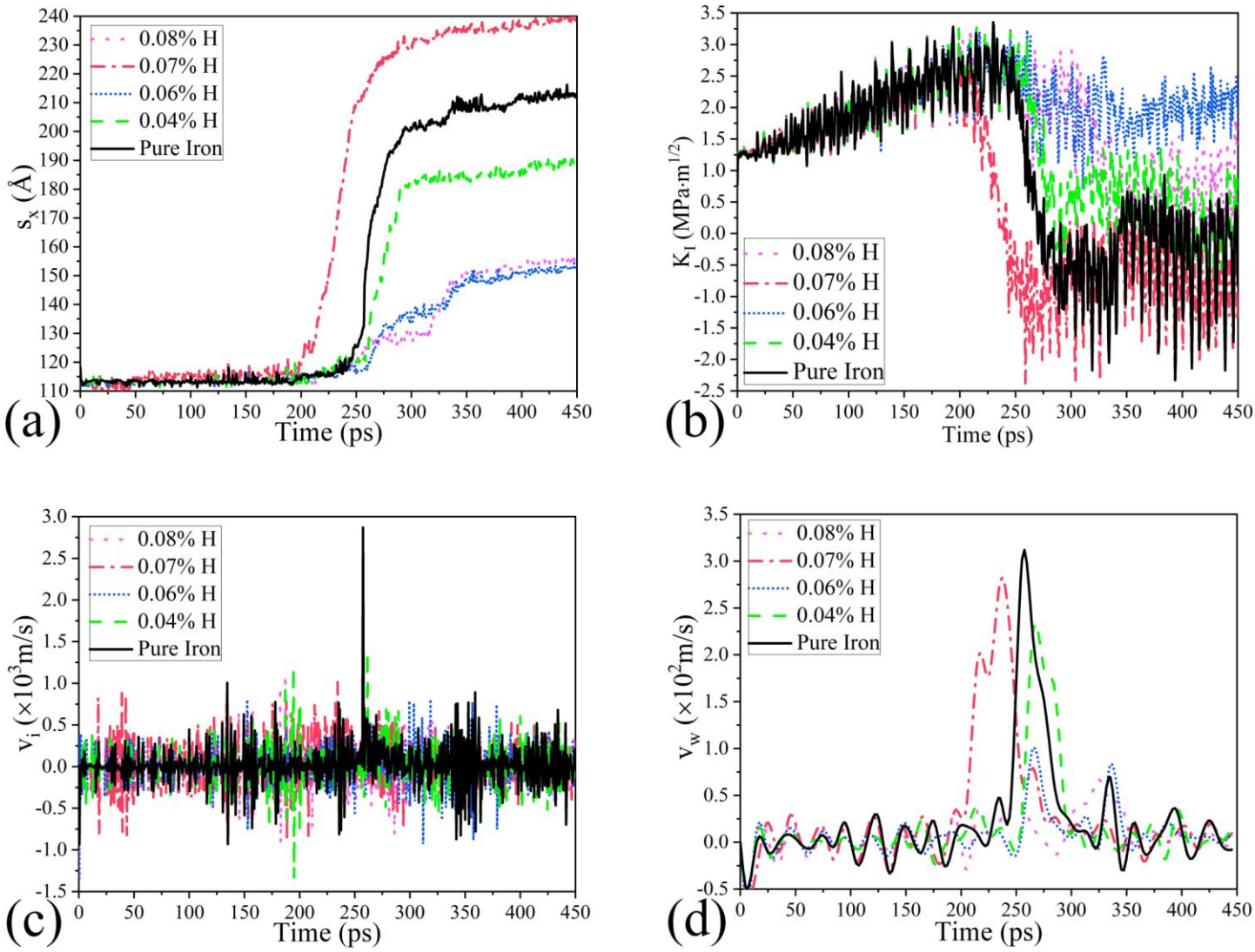

Fig. 3 Crack propagation. (a) Propagated cracks along the [100] direction. HE occurred when C_H=0.07%. (b) The stress intensity factor for mode-I fracture. (c) The oscillation of the instantaneous velocity v_i of the crack. (d) The decrement of averaged velocity v_w by dissolved hydrogen, and the earlier crack extension with a longer unstable duration at C_H=0.07%.

Table 1 Critical stress intensity factors

C_H (%)	K_{IC} (MPa·m$^{1/2}$)	Time (ps)
0.0	3.354	230
0.04	3.273	230
0.06	3.243	215
0.07	3.097	194
0.08	3.264	209.5

Fig. 3(c) shows the high-frequency oscillation of v_i, representing the opening and closing of cracks that occur alternately, due to the elasticity and the interaction between neighbors. To observe the effect on crack propagation clearly, we sampled v_i to v_w. Fig. 3(d) shows that, if v_w approaches the sound speed in the air, it will be maintained during the crack's unstable propagation. Dissolved hydrogen can suppress the crack's rapid growth by decreasing the maximum of v_w, but it can also advance or delay the acceleration (as shown as C_H = 0.07% and C_H = 0.04% in Fig 3(d), respectively), or extend the duration of unstable propagation (as shown as C_H = 0.07% in Fig 3(d)), as HE occurred at C_H = 0.07%.

3.1.2 Structural evolutions

Hydrogen-enhanced dislocation emission [6,7,21,32,52] is also observed in this work. However, it had little impact on fractures. Fig. 4(a) showed that 1/2<111> dislocations emitted earlier at C_H > 0, but were still later than the crack's unstable propagation or slight closure (with C_H = 0.04%), as shown in Fig. 3(a). Therefore, these dislocations only relax the cracks. The <100> dislocation should accelerate the fracture, which contributes little to plasticity [80]; however, it only strengthens at 23.5 ps when C_H = 0.07% as a result of pinning the crack by a nearby hydrogen atom, and not even occurs when C_H = 0.08%, such emission has little help for fracture; see Fig. 4(b-d).

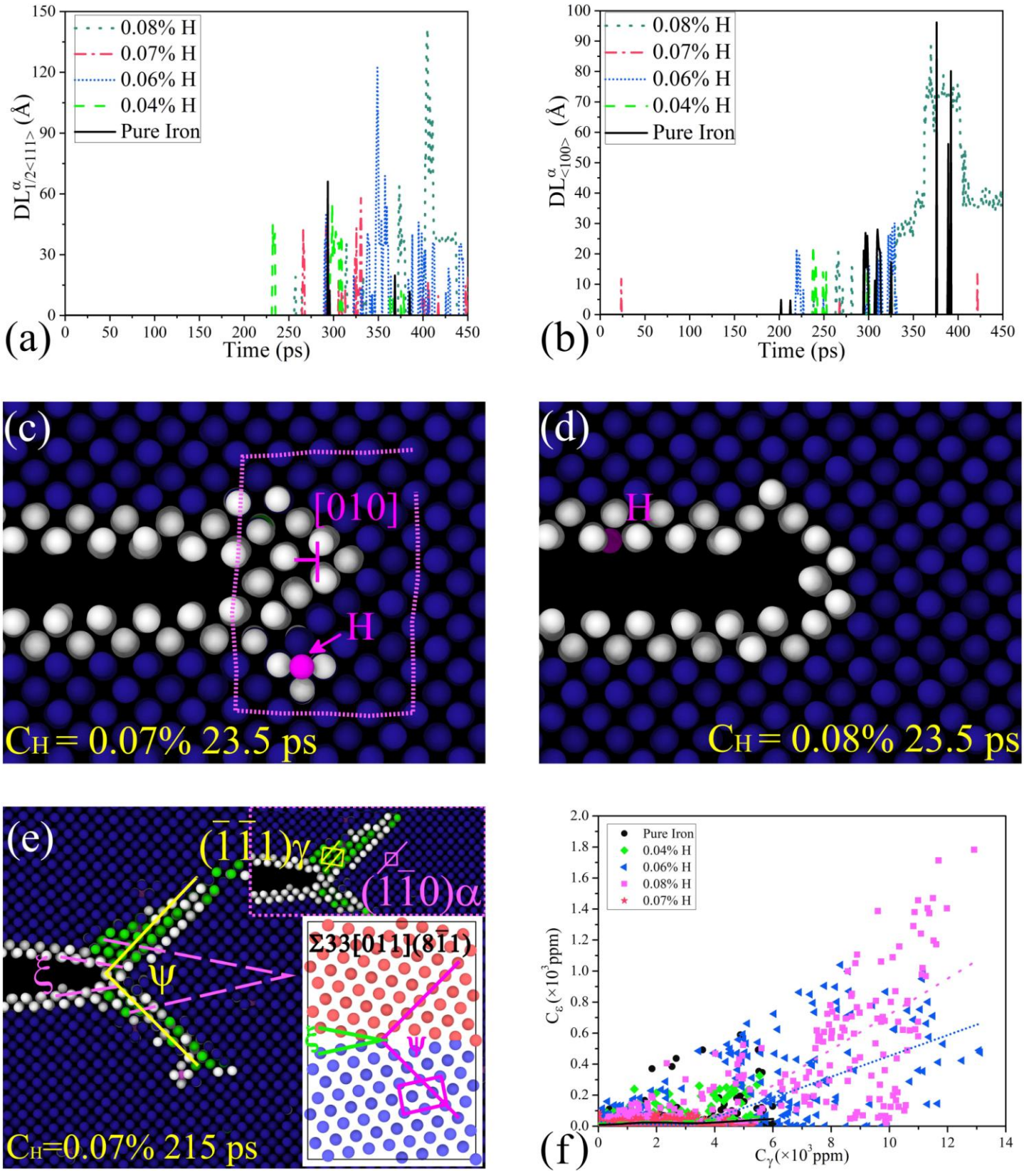

Fig. 4 Dislocations emission and structural evolutions. (a)Hydrogen enhanced the 1/2<111> dislocations emission. (b) Hydrogen influences the <100> dislocations emission. (c) Pinning the crack caused the [010] dislocation when C_H = 0.07% at 23.5 ps, by the nearby H atom. (d) The crack tip at 23.5 ps when C_H = 0.08%. (e) The orientation

relationship (OR) of the γ and the α phases with C_H = 0.07% at 215ps, and the formed structure like the Σ33[011](8$\bar{1}$1) grain boundary (GB). (f) Hydrogen influenced the strain-induced MT and enhances the formation of γ and ε phases, except for C_H = 0.07%.

The orientation relationship (OR) between the α and γ phases was [001]α//[011]γ and (1$\bar{1}$0)α//($\bar{1}\bar{1}$1)γ, subjected to Nishiyama-Wassermann (N-W) OR [81]. This is the same as found in our previous work [60], but structures like grain boundaries (GBs) form continuously when C_H = 0.07%. For example, a Σ33[011](8$\bar{1}$1)γ GB-like structure was formed with ξ = 20.05° and ψ = 90° at 215 ps, as shown in Fig. 4(e). Since hydrogen segregation [82] and migration [83], and fracture tend to occur along GBs [18,26,82,83], the resulting structures promote HE and may lead to AIDE favorable for hydrogen adsorption [7]. When C_H > 0, the γ→ε transformation was also observed, following the Olsen-Cohen model [84–87]. As shown in Fig. 4(f), using LWR [76] to fit the curves in most models, the γ and ε phases increase with C_H, while the promoted HE suppresses the phase transformation at C_H = 0.07%. A debate about whether the dissolved hydrogen can stabilize the ε phase continues [38,41], and our scattering results in Fig. 4(f) show that the ε phase increases faster, but is still unstable.

3.1.3 Fracture and hydrogen distribution

Fig. 5(a,b) shows the cracks and phases affected by internally dissolved hydrogen atoms at 242 ps. In the model of C_H > 0, the planarity of slips and stress concentration occurred, in which {112}<111> slip was suppressed, and the γ phase grew along the {110} plane. In the model with C_H = 0.07%, the area with the highest concentration of stress is the smallest, and the crack is the longest. The relaxation in the larger area in the model also reduces the phase transition.

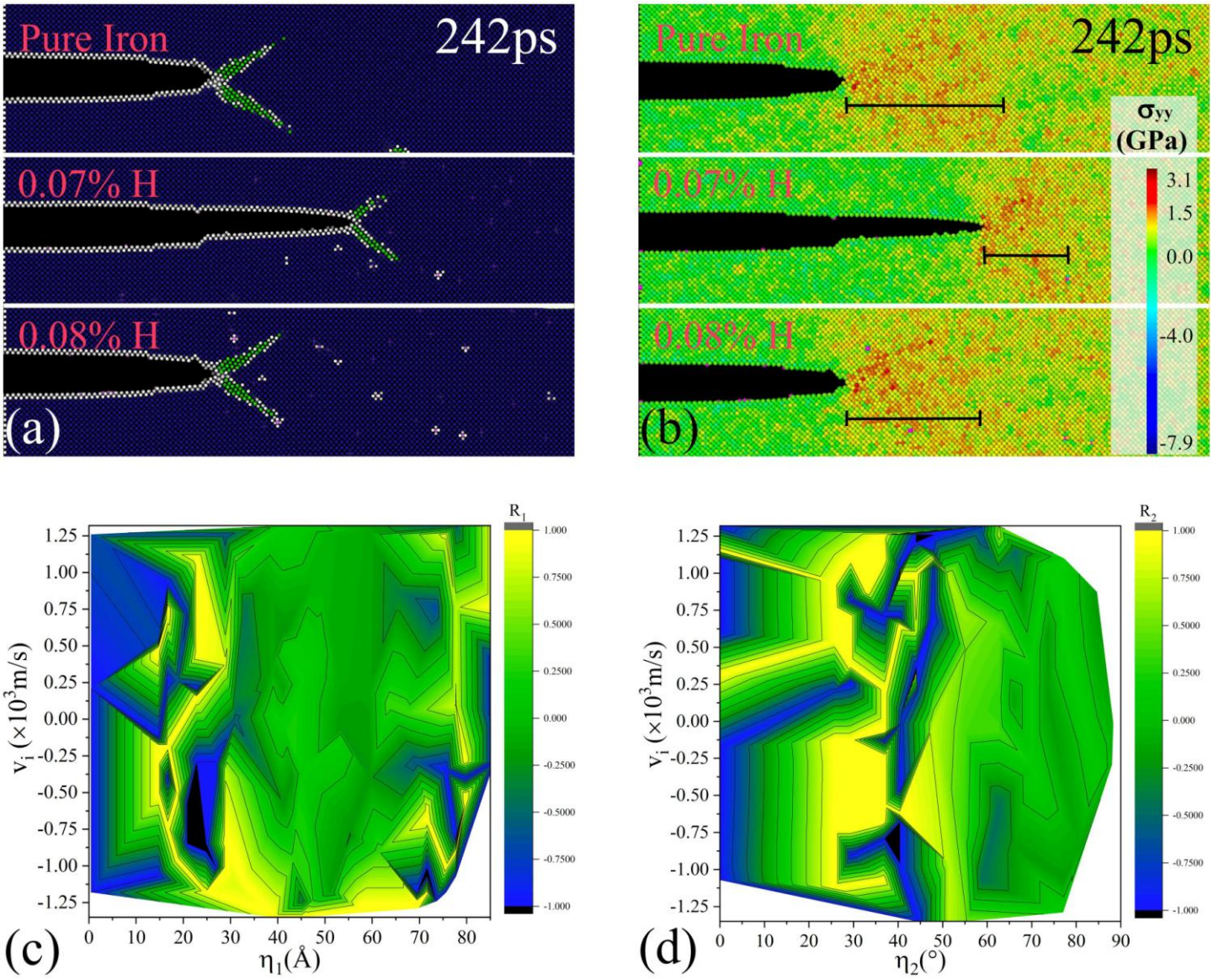

Figure 5. Effect of hydrogen on the fracture. (a) Crack extension and γ phase at 242ps. (b) Stress distribution at 242 ps. (c) The correlation between η_1 and v_i. (d) The correlations between η_2 and v_i of cracks.

Since high loading rates affect dislocation emission and hydrogen migration [88–90], cracks in MD simulations are mainly affected by nearby hydrogen atoms. Tab. 2 shows the effect represented by the combination of v_i and R_j, where R_j represents the Pearson coefficient of v_i and η_j [68,91]. $R_j > 0$ or $R_j < 0$ indicates whether the crack is promoted or suppressed, and $v_i > 0$ or $v_i < 0$ indicates that the crack grows or closes.

Table 2 Crack extension and closure with v_i and R_j

v_i	R_j	Influence on crack
>0	>0	Promote extension
>0	<0	Suppress extension
<0	<0	Promote closure
<0	>0	Suppress closure

Fig. 5(c) shows the effect of hydrogen on the fracture at different distances from the crack tip, as the most relevant area is at 0-40Å from the crack tip, which is more pronounced in the three intervals: when η_1 < 10 Å, hydrogen suppresses crack propagation and promotes closure, due to hydrogen dissolution induced stress relaxation; for $\eta_1 \in (10,20)$ Å, hydrogen inhibits crack propagation and closure by relaxing stress and causing decohesion, respectively; for $\eta_1 \in$ (20,30) Å, hydrogen promotes crack propagation and closure, because the same slip system can be activated in opposite directions by different crack motions. Song and his colleagues reported that HE could be induced by stress concentration with inhibited dislocation emission [25,54]. Their results are consistent with HEDE, which were caused by hydrogen atoms inserted 10 Å near the crack tip and the high local C_H. Our work differs from theirs with much lower C_H. We surmise that HELP relates to both HE and MT. It is well known that {112}<111> and {110}<111> are the preferred slip systems activated at low and room temperatures, respectively [33,92]. We observed that their activation had induced $\alpha \rightarrow \gamma$ MT [60]; however, Fig. 5(d) shows that they also relate to HE. For η_2 < 15°, hydrogen near the cracking direction inhibits fracture by suppressing crack propagation and promoting its closure. For $\eta_2 \in (20°,40°) \cup (50°,65°)$, hydrogen promotes crack propagation and inhibits its closure. Since the intersections of some {112} planes with the (001) plane form angles of about 26° with the [100] or [010] direction, hydrogen atoms near the {112}<111> slip system will promote fracture. Similarly, for $\eta_2 \sim 45°$, caused by hydrogen atoms on the slip system

of {110}<111>, crack propagation is suppressed, and closure is promoted. With the increment of C_H, the unstable stacking fault energy (γ_{us}) increases in the {112}<111> slip system but decreases in the {110}<111> slip system [93]; therefore the activated slip system and stress relaxation will affect the fracture together. As we observed, hydrogen in the {112}<111> slip system promotes HE by suppressing the {112}<111> slips, and in the {110}<111> slip system promotes MT by promoting the {110}<111> slips.

3.2 The influences of adsorbed hydrogen atoms on mode-I fractures of α-Fe single crystal

3.2.1 Crack propagation and the structure evolution near the crack tip

Fig. 6 shows the crack growth of pure iron through MD+tfMC. As shown in Fig. 6(a), when the simulation starts, the pre-crack closure occurs accompanied by swallowing the disordered structure at crack front. This is because the loading rate decreases with the increasing time scale of tfMC [55], thereby reducing the stress concentration near the crack tip. As shown in Fig. 6(b), the crack did not extend apparently until the 11th loading, but then propagated rapidly to its initial length with the formation of the γ phase and stabilized with a strain $\varepsilon_L = 2.519\%$ along the [010]α direction. Fig. 6(c) shows that, until the 14th loading, the cracks slowly propagated again and continued until the end of the simulation.

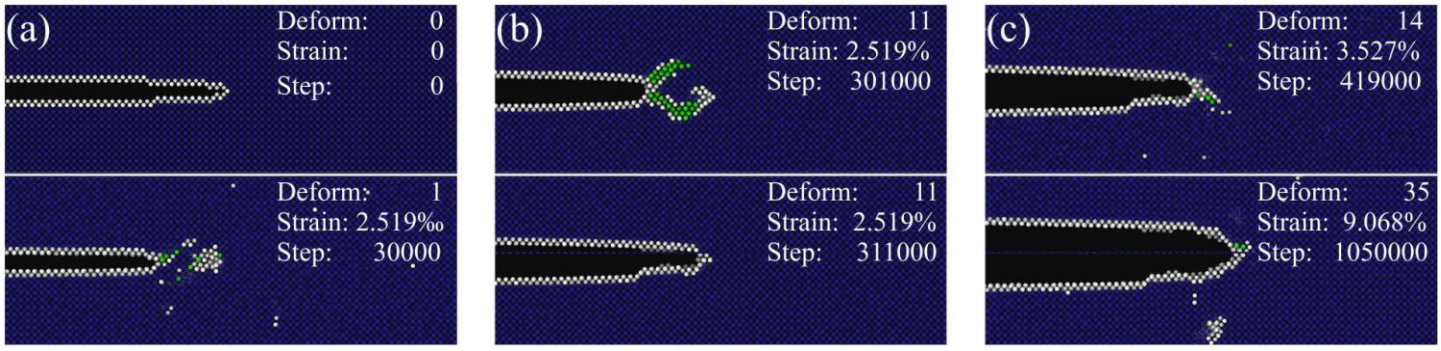

Fig. 6 Crack propagation of pure iron by MD+tfMC simulation. (a) Initial state and closure of the crack. (b) The crack state and MT under the 11-th loading. (c) Slow propagation of the crack, until the 14-th loading.

Fig. 7 shows the α-Fe model tensioned with adsorbed hydrogen atoms (colored in pink). As shown in Fig. 7(a), the crack did not propagate obviously until the 12th load, but thereafter the γ phases were formed and quickly disappeared alternately. However, when ε_L = 3.527% and at the 14th tension shown in Fig. 7(b), the structure changed rapidly in front of the crack. At step 2,668,000, a large amount of amorphization occurs, which rapidly expanded in a zone in front of the γ phase in [110]α direction (marked as Z-A), and engulfed the crack tip until the subsequent step 2,671,000. Fig. 7(c,d) shows the evolution of voids. In step 2,676,000, the void nucleated and grew rapidly in Z-A, and had shortly formed γ and ε phases. This growth stopped at step 2,715,000, and the structure was converted back to the α phase between the crack tip and the void (marked as Z-I). Then, the atoms in Z-I remained ordered until the 25th load, and, from step 4,733,000, with the change of the crack propagation direction to [110]α, the void grew again. From step 6,034,000, after ε_L = 8.061%, rapid crack growth occurred in connection with the void, and the activated $(\dot{1}10)[11\dot{1}]$ and $(\dot{1}10)[111]$ slips led to the changes in the [110]α direction, with $(\dot{1}10)\cap(001)=[110]$.

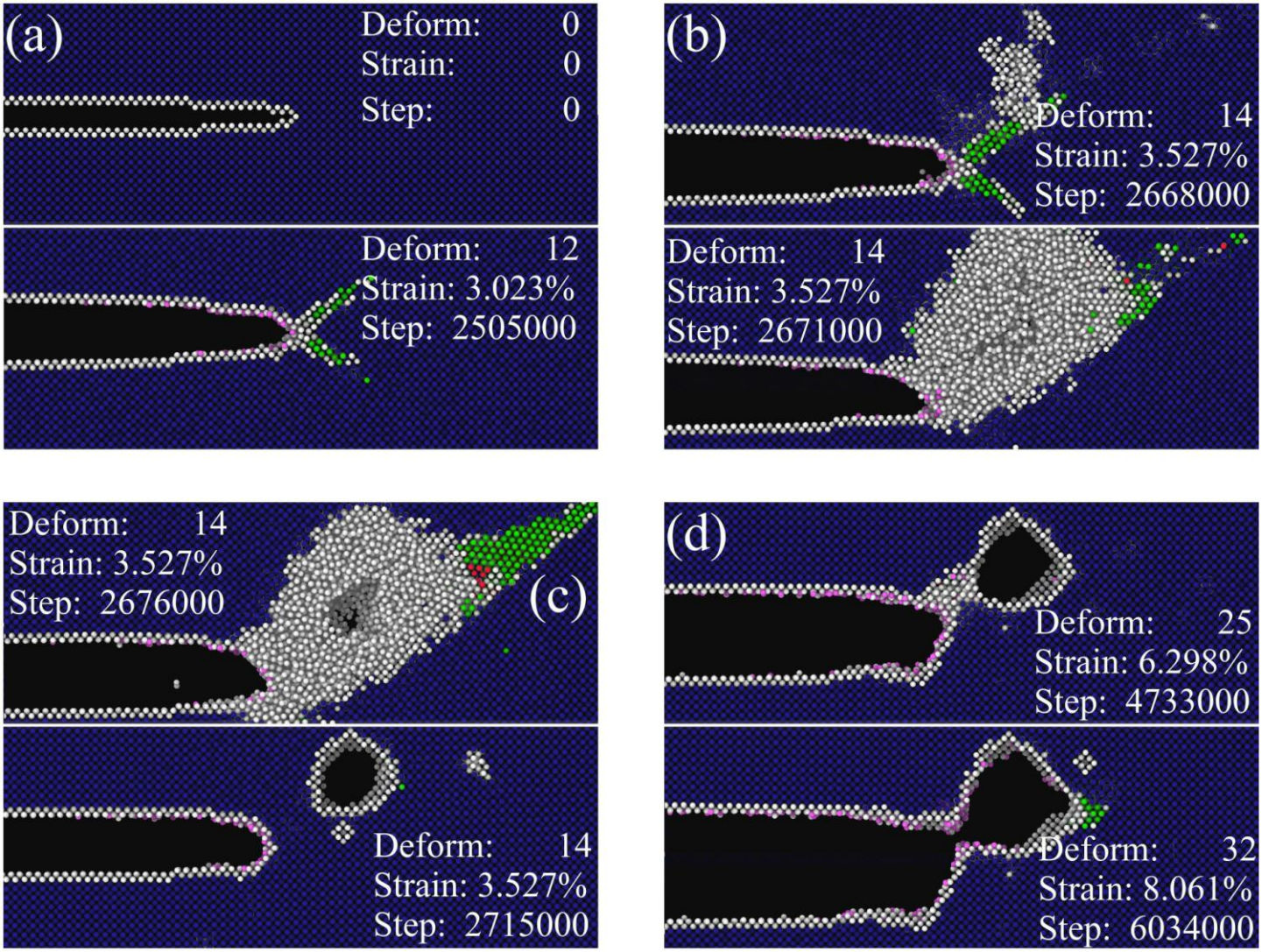

Fig. 7 Crack propagation with adsorbing hydrogen atoms. (a) Initial status and propagation of the crack, with the formation and disappearance of the γ phases from the 12th loading. (b) The Z-A zone with amorphization and disappearance of the γ phase. (c) The nucleation and growth of the void happened in Z-A. (d) The equilibrated void grew again and the rapid crack propagation with a changing direction.

Fig. 8(a) shows the simulation results of α-Fe MD (marked as Fe-M), α-Fe MD+tfMC (marked as Fe-t), and MD+tfMC (marked as H-t, in which gradually inserting hydrogen as the adsorbed atoms in α-Fe). It can be seen that under Fe-M, the crack started to propagate rapidly from the strain ε_L = 3.7785% and exhibited brittle cleavage characteristics, while in the other two cases, the growth was very slow, and closure even happened at the beginning of the crack under Fe-t. With H-t, the

pre-crack closure was suppressed, but the crack hardly propagated until ε_L = 7.557%. Although the fracture was promoted in the case of small loads with very few hydrogen atoms before the strain reached ε_L = 3.527%, it was inhibited with higher C_H thereafter. The closure of the crack at the strain $\varepsilon_L \in$ (3.527%, 3.7855%) caused the crack propagation to lag behind that under H-t, which shows that the locally increased C_H suppressed the fracture. Fig. 8(b) and Fig. 7(c) show that the nucleation and growth of the void in Z-A also suppressed the fracture at ε_L = 3.527%. The void maintained its volume after quickly equilibrium until ε_L = 6.298%, but eventually results in the sudden rupture when ε_L = 7.557%, with microvoid-coalescence (MVC) by connecting the void and the crack.

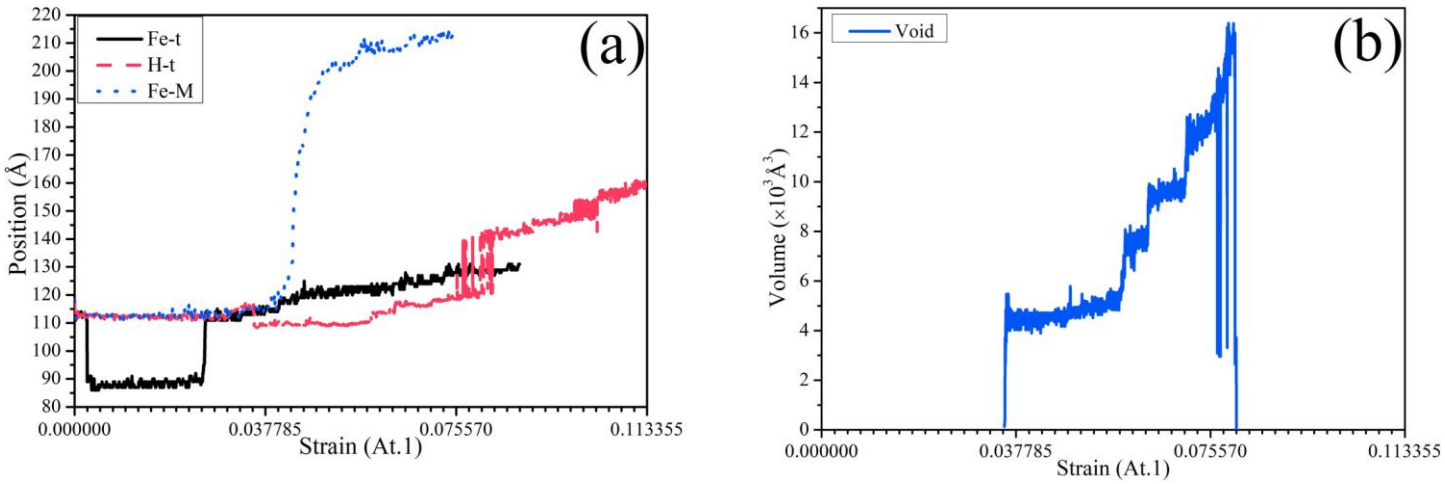

Fig. 8 Crack propagation and volume evolution of voids. (a) Crack propagation with Fe-M, Fe-t, and H-t. The addition of hydrogen inhibited the crack closure and propagation at an early stage, until the strain increased to 7.557%. (b) The void volume with H-t.

Fig. 9 shows the counting of different phases with Fe-t and H-t. At the beginning, the gradually inserted hydrogen atoms might decrease the tensile stress near the crack tip, thereby inhibited the disordering and structural transformation. At ε_L = 3.527%, the γ, ε phases and disordered structure increased, and the disordered structure accounted for the largest proportion. After ε_L = 3.7785%, count of the γ and ε phases suddenly dropped, which happened with the nucleation of the void.

This amorphization which occurs with strongly localized plasticity and promotes

the latter's void nucleation. As shown in Fig. 8 (a), this is due to the cumulative tension in the [110]α direction, caused by suppressing the crack propagation by hydrogen atoms near the crack tip.

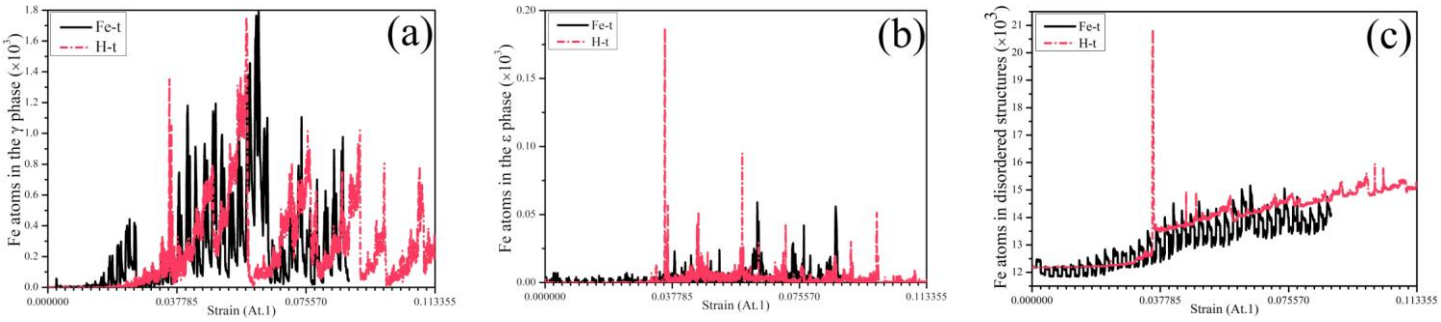

Fig. 9 Counting iron atoms for different phases with Fe-t and H-t. The formation of γ, ε phases and the disordered structure were all suppressed until ε_L = 3.527%, and they were suddenly dropped at ε_L = 3.7785% . (a) Count for the γ phase. (b) Count for the ε phase. (c) Count for the amorphization structure.

3.2.2 Hydrogen distribution and stress

Plasticity phenomena usually occur with HE, for example: MVC fracture [21], voids and the symmetrically distributed micro-cracks on both sides of the slip band in α-Fe [33], significantly enhanced strain-induced vacancies [46], and voids nucleation in front of the crack tip before cracks propagate in pipeline steel [49]. As similar phenomena were observed in this work, to discuss their relationships, we analyzed the hydrogen distribution and stress changes.

The first peak of g(r) from Eq. (23) represents the distance between the nearest neighbors [94]. Fig. 10(a) shows that d_m > 2.1 Å, until the 14th load; and $d_m \geq$ 1.8 Å, with the lattice relaxed due to the void nucleation and growth. As shown in Fig. 8 (b), after the 24th load, d_m returned to about 2.1 Å, consistent with the DFT results [54] and caused by the resumption of void growth. There is no consensus on the location of hydrogen atoms distributed. Hashimoto et al. believed that internal C_H was more important for HE [30]. Hancock et al. believed that fractures were affected by hydrogen atoms on the crack surfaces [34,50], and Lynch believed that hydrogen atoms near the crack tip could cause micro-voids [6,7]. The statistical hydrogen

distribution f_H in Fig. 10(b) shows that most hydrogen atoms are located within 6.4Å (about four times the distance between a Tet-site and an iron atom) of the fracture surface, which indicates that hydrogen diffusion mainly occurs near such a surface. As described above, fractures will be suppressed when $\eta_1 < 10$ Å, which explains why fractures are suppressed when $\varepsilon_1 < 7.557\%$ with H-t, as shown in Fig. 8(a). Due to local expansion, a small number of hydrogen atoms diffused to a further location after the 17th loading and $\varepsilon_L > 4.282\%$, which shows that the amorphization is indeed caused by the hydrogen-induced strain localization [3,37]. However, voids formed in this work have little relationship to the hydrogen-vacancy recombination effect.

As the location of the crack tip is (x_t, y_t)Å, the area $x \in [x_t, x_t+10]$Å, $y \in [y_t-5, y_t+5]$Å is marked as Z-t, which is the area closest to the crack front. The area $x \in [x_t+20, x_t+35]$Å, $y \in [y_t+10, y_t+36]$Å is marked as Z-II, which is the forming area of voids. After defining these two areas, we mark the area between the crack and the void as Z-I. Fig. 10(c,d) shows the results of σ_{max} and τ_{max} in different regions of Fe-t and H-t. As shown in the figure, hydrogen significantly reduces σ_{max} and τ_{max} of Z-t and Z-II regions under small loading conditions. As mentioned above, low C_H hydrogen atoms relaxed the stress field near the crack tip, which temporarily suppressed shear slip and crack propagation. This relaxation caused stress concentration and shear slip localization at farther locations. When loading continued, it caused a linear increase of stress in Z-II, and quickly exceeded the results of Fe-t. Therefore, when $\varepsilon_L = 3.527\%$, nucleation and growth of the void occurred. The void relaxed structures in Z-II, but the stress was still highly concentrated in Z-I (for σ_{max}, even increasing to 9 GPa), which provided a driving force for the rapid growth of voids, and suddenly relaxed after equilibrium. σ_{max} and τ_{max} in Z-I increased with the subsequent loading. When σ_{max} again increased to around 9 GPa, the crack extended and void growth resumed. Since hydrogen enhanced τ_{max} in Z-t, the plastic localization was enhanced. When $\varepsilon_L = 7.557\%$, voids and cracks were suddenly connected, and Z-I and Z-t were significantly reduced. It can be seen from Fig. 10(b,c) that a small number of hydrogen atoms were able to diffuse deeper in the matrix only

when the tensile stress in Z-I is large enough. The hydrogen atoms in Z-t caused the nucleation and growth of voids in Z-II before they diffused into the matrix. Fig. 10(d) shows the cause of amorphization and void formation. With the influence of hydrogen on τ_{max}, the plasticity of Z-t was initially suppressed, but the plasticity of Z-II was enhanced after a few loadings. We observed hydrogen-induced strain localization and void nucleation and growth, which was similar to HESIV, with the exception of the hydrogen-void combination. In our work, MVC was caused by the strain localization and the accumulated tensile stress in the matrix. This is because the hydrogen absorbed in crack front inhibits crack propagation.

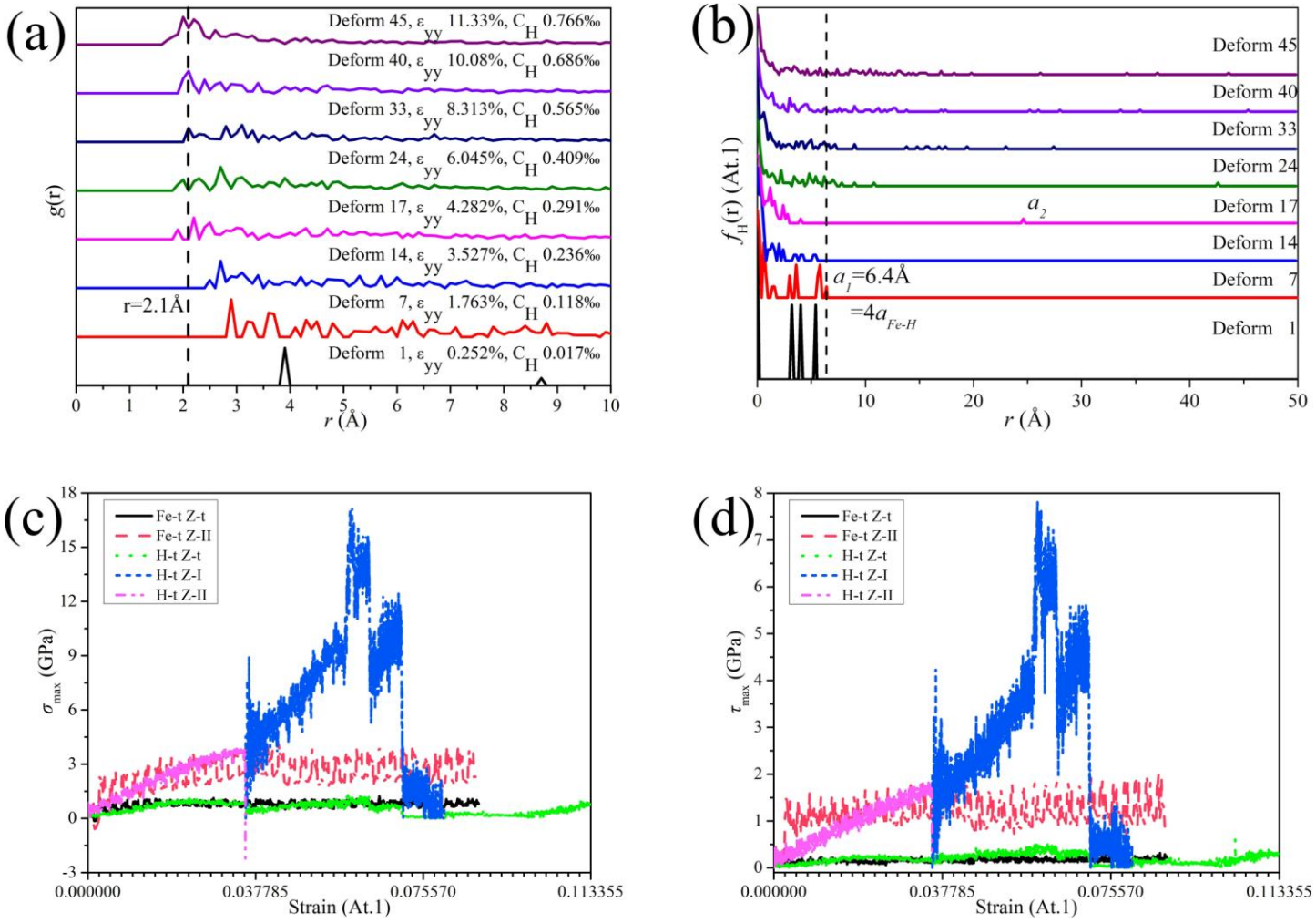

Fig. 10 Hydrogen distribution and stresses in different regions. (a) PCF of hydrogen atoms. The first peak denoted d_m, is mostly higher than 2.1Å. (b)The distances from the hydrogen atoms to the crack surface. Most of which are less than 6.4 Å. (c) The average maximum principal stress. σ_{max} is linearly increases in Z-II at the beginning, and

concentrates in Z-I when void nucleated. Which promotes the void growth by consuming itself; therein lies the following slowly growth of the void until the crack connecting. (d)Average maximum shear stress τ_{max}. Which is similar to $\sigma_{max.}$

4. Conclusions

The (010)[100] pre-cracked models of the α-Fe single crystal specimen were simulated, in which dissolved hydrogen atoms were in four low C_H (maximum 14.3 wppm). Through the analysis of crack propagation and structure, the statistical results were used to study the effect of hydrogen atom distribution near the crack tip on fracture. Then, the local structure, hydrogen distribution and stress effects of the mode-I fracture with adsorbed hydrogen atoms were analyzed by MD+tfMC. Here we draw the following conclusions:

(1) The local hydrogen distribution influenced on the HE of α-Fe single crystal, and the dissolved and adsorbed hydrogen atoms can partially cause HE, which, in turn, is partly based on HELP and HESIV.

(2) In the (010)[100] fracture of α-Fe single crystal, the internal hydrogen atoms will localize the shear and slip. This phenomenon will promote or inhibit the HE, depending on where the hydrogen atoms are located.

(3) The hydrogen atoms located on the {112} plane suppress the {112}<111> slips, and then promote HE by generating GB-liks microstructures, which is beneficial to the fracture and possibly to AIDE.

(4) Hydrogen atoms located on the {110} planes promote the {110}<111> slips, and then inhibit HE by competing with the fracture to enhance MT.

(5) Hydrogen atoms located in front of the (010)[100] crack and within the range of 10 Å around the crack tip suppress HE.

(6) Hydrogen atoms adsorbed from the outside of the crack will promote HE with MVC by causing nucleation and growth of voids on the {110} planes. Strain localization and the void formation are similar to HESIV, except that the voids are caused by tensile stress accumulated in the matrix, because the accumulated

hydrogen suppresses early crack propagation and shear through the stress relaxation near crack front.

Acknowledgments

This work is funded by the National Natural Science Foundation of China (Grant No. 11174030, 51701171). The authors acknowledge the foundation for financial support.

References:

[1] Johnson WH, Thomson W. II. On some remarkable changes produced in iron and steel by the action of hydrogen and acids. Proc R Soc London 1875;23:168–79. https://doi.org/10.1098/rspl.1874.0024.

[2] Hanson JP. The role of grain boundary character in hydrogen embrittlement of nickel-iron superalloys. Massachusetts Institute of Technology, 2016.

[3] Nagumo M. Fundamentals of hydrogen embrittlement. 2016. https://doi.org/10.1007/978-981-10-0161-1.

[4] Robertson IM, Sofronis P, Nagao A, Martin ML, Wang S, Gross DW, et al. Hydrogen Embrittlement Understood. Metall Mater Trans A 2015;46:2323–41. https://doi.org/10.1007/s11661-015-2836-1.

[5] Troiano AR. The Role of Hydrogen and Other Interstitials in the Mechanical Behavior of Metals. Metallogr Microstruct Anal 2016;5:557–69. https://doi.org/10.1007/s13632-016-0319-4.

[6] Lynch SP. Metallographic contributions to understanding mechanisms of environmentally assisted cracking. Metallography 1989;23:147–71. https://doi.org/https://doi.org/10.1016/0026-0800(89)90016-5.

[7] Lynch S. Hydrogen embrittlement phenomena and mechanisms. Corros Rev 2012;30:105–23. https://doi.org/10.1515/corrrev-2012-0502.

[8] Zapffe CA, Sims C. Hydrogen, flakes and shatter cracks. Met Alloy 1940;12:145–51.

[9] Flanagan TB, Mason NB, Birnbaum HK. The effect of stress on hydride precipitation. Scr Metall 1981;15:109–12. https://doi.org/https://doi.org/10.1016/0036-9748(81)90148-4.

[10] Ma XQ, Shi SQ, Woo CH, Chen LQ. The phase field model for hydrogen diffusion and γ-hydride precipitation in zirconium under non-uniformly applied stress. Mech Mater 2006;38:3–10. https://doi.org/10.1016/J.MECHMAT.2005.05.005.

[11] Shih DS, Robertson IM, Birnbaum HK. Hydrogen embrittlement of α titanium: In situ tem studies. Acta Metall 1988;36:111–24. https://doi.org/10.1016/0001-6160(88)90032-6.

[12] Bair J, Asle Zaeem M, Tonks M. A review on hydride precipitation in zirconium alloys. J Nucl Mater 2015;466:12–20. https://doi.org/10.1016/J.JNUCMAT.2015.07.014.

[13] Polyanskii AM, Polyanskii VA, Yakovlev YA. Metrological Assurance of Measurement of Hydrogen Concentration in Metals – a Basis for Safety in the Oil and Gas Industry. Meas Tech 2013;56:328–33. https://doi.org/10.1007/s11018-013-0204-3.

[14] ARIA. Hydrogen tank explosion in a chemical plant 2017:1–5. https://www.aria.developpement-durable.gouv.fr/fiche_detaillee/437_en-2/?lang=en.

[15] ARIA. Major release of gas from bleeders in a steel plant 2016. https://www.aria.developpement-durable.gouv.fr/accident/48395_en/?lang=en.

[16] Khare A, Vishwakarma M, Parashar V. A review on failures of industrial components due to hydrogen embrittlement & techniques for damage prevention. Int J Appl Eng Res 2017;12:1784–92.

[17] Chatzidouros E V., Traidia A, Devarapalli RS, Pantelis DI, Steriotis TA, Jouiad M. Fracture toughness properties of HIC susceptible carbon steels in sour service conditions. Int J Hydrogen Energy 2019;44:22050–63. https://doi.org/10.1016/j.ijhydene.2019.06.209.

[18] Koyama M, Akiyama E, Lee YK, Raabe D, Tsuzaki K. Overview of hydrogen

embrittlement in high-Mn steels. Int J Hydrogen Energy 2017;42:12706–23. https://doi.org/10.1016/j.ijhydene.2017.02.214.

[19] Chen Y, Zheng S, Zhou J, Wang P, Chen L, Qi Y. Influence of H2S interaction with prestrain on the mechanical properties of high-strength X80 steel. Int J Hydrogen Energy 2016;41:10412–20. https://doi.org/10.1016/j.ijhydene.2016.01.144.

[20] Oriani RA. The Physical and Metallurgical Aspects of Hydrogen in Metals. Fourth Int. Conf. Cold Fusion, Hillview Ave., Palo Alto: Lahaina, Maui: Electric Power Research Institute; 1993.

[21] Beachem CD. A new model for hydrogen-assisted cracking (hydrogen "embrittlement"). Metall Mater Trans B 1972;3:441–55. https://doi.org/10.1007/BF02642048.

[22] Oriani RA. Hydrogen Embrittlement of Steels. Annu Rev Mater Sci 1978;8:327–57.

[23] Song EJ, Bhadeshia HKDH, Suh D-W. Effect of hydrogen on the surface energy of ferrite and austenite. Corros Sci 2013;77:379–84. https://doi.org/https://doi.org/10.1016/j.corsci.2013.07.043.

[24] Song J, Curtin WA. Mechanisms of hydrogen-enhanced localized plasticity: An atomistic study using alpha-Fe as a model system. ACTA Mater 2014;68:61–9.

[25] Song J, Curtin WA. A nanoscale mechanism of hydrogen embrittlement in metals. Acta Mater 2011;59:1557–69.

[26] Pfeil LB. The effect of occluded hydrogen on the tensile strength of iron. J Franklin Inst 1927;203:331–2. https://doi.org/10.1016/s0016-0032(27)92466-1.

[27] PETCH NJ, STABLES P. Delayed Fracture of Metals under Static Load. Nature 1952;169:842–3.

[28] Itsumi Y, Ellis DE. Electronic bonding characteristics of hydrogen in bcc iron: Part I. Interstitials. J Mater Res 1996;11:2206–13.

[29] Fu L, Fang H. Atomistic investigation of hydrogen embrittlement effect for symmetric and asymmetric grain boundary structures of bcc Fe. Comput Mater

Sci 2019;158:58–64.

[30] Hashimoto M, Latanision RM. The role of dislocations during transport of hydrogen in hydrogen embrittlement of iron. Metall Trans A 1988;19:2799–803. https://doi.org/10.1007/BF02645814.

[31] Wang S, Martin ML, Sofronis P, Ohnuki S, Hashimoto N, Robertson IM. Hydrogen-induced intergranular failure of iron. Acta Mater 2014;69:275–82. https://doi.org/https://doi.org/10.1016/j.actamat.2014.01.060.

[32] Hirth JP. Effects of hydrogen on the properties of iron and steel. Metall Trans A 1980;11:861–90. https://doi.org/10.1007/BF02654700.

[33] Hinotani S, Ohmori Y, Terasaki F. Hydrogen crack initiation and propagation in pure iron single crystal. Mater Sci Technol (United Kingdom) 1994;10:141–8. https://doi.org/10.1179/mst.1994.10.2.141.

[34] Vehoff H. Hydrogen related material problems BT - Hydrogen in Metals III: Properties and Applications. In: Wipf H, editor., Berlin, Heidelberg: Springer Berlin Heidelberg; 1997, p. 215–78. https://doi.org/10.1007/BFb0103404.

[35] Kimura A, Kimura H. Hydrogen embrittlement in high purity iron single crystals. Mater Sci Eng 1986;77:75–83. https://doi.org/https://doi.org/10.1016/0025-5416(86)90355-1.

[36] Matsui H, Kimura H, Moriya S. The effect of hydrogen on the mechanical properties of high purity iron I. Softening and hardening of high purity iron by hydrogen charging during tensile deformation. Mater Sci Eng 1979;40:207–16. https://doi.org/10.1016/0025-5416(79)90191-5.

[37] Nagumo M, Takai K. The predominant role of strain-induced vacancies in hydrogen embrittlement of steels: Overview. Acta Mater 2019;165:722–33.

[38] Narita N, Altstetter CJ, Birnbaum HK. Hydrogen-related phase transformations in austenitic stainless steels. Metall Trans A 1982;13:1355–65. https://doi.org/10.1007/BF02642872.

[39] Rigsbee JM. TEM observations on hydrogen-induced ϵ-HCP martensite. Metallography 1978;11:493–8. https://doi.org/https://doi.org/10.1016/0026-0800(72)90074-2.

[40] Murakami Y. The effect of hydrogen on fatigue properties of metals used for fuel cell system BT - Advances in Fracture Research. In: Carpinteri A, Mai Y-W, Ritchie RO, editors., Dordrecht: Springer Netherlands; 2006, p. 167–95.

[41] Głowacka A, Woźniak MJ, Nolze G, Świątnicki WA. Hydrogen induced phase transformations in austenitic-ferritic steel. Solid State Phenom 2006;112:133–40. https://doi.org/10.4028/www.scientific.net/SSP.112.133.

[42] Mogilny GS, Teus SM, Shyvanyuk VN, Gavriljuk VG. Plastic deformation and phase transformations in austenitic steels in the course of hydrogen charging and subsequent mechanical tests. Mater Sci Eng A 2015;648:260–4. https://doi.org/https://doi.org/10.1016/j.msea.2015.09.015.

[43] Sofronis P, Robertson IM. Transmission electron microscopy observations and micromechanical/continuum models for the effect of hydrogen on the mechanical behaviour of metals. Philos Mag A Phys Condens Matter, Struct Defects Mech Prop 2002;82:3405–13. https://doi.org/10.1080/01418610208240451.

[44] Ferreira PJ, Robertson IM, Birnbaum HK. Hydrogen effects on the interaction between dislocations. Acta Mater 1998;46:1749–57. https://doi.org/10.1016/S1359-6454(97)00349-2.

[45] Turnbull A. Hydrogen diffusion and trapping in metals. Gaseous Hydrog Embrittlement Mater Energy Technol 2012:89–128. https://doi.org/10.1533/9780857095374.1.89.

[46] Sakaki K, Kawase T, Hirato M, Mizuno M, Araki H, Shirai Y, et al. The effect of hydrogen on vacancy generation in iron by plastic deformation. Scr Mater 2006;55:1031–4. https://doi.org/https://doi.org/10.1016/j.scriptamat.2006.08.030.

[47] Li S, Li Y, Lo Y-C, Neeraj T, Srinivasan R, Ding X, et al. The interaction of dislocations and hydrogen-vacancy complexes and its importance for deformation-induced proto nano-voids formation in α-Fe. Int J Plast 2015;74:175–91.

[48] Awane T, Fukushima Y, Matsuo T, Murakami Y, Miwa S. Highly sensitive

secondary ion mass spectrometric analysis of time variation of hydrogen spatial distribution in austenitic stainless steel at room temperature in vacuum. Int J Hydrogen Energy 2014;39:1164–72. https://doi.org/10.1016/j.ijhydene.2013.10.116.

[49] Neeraj T, Srinivasan R, Li J. Hydrogen embrittlement of ferritic steels: Observations on deformation microstructure, nanoscale dimples and failure by nanovoiding. Acta Mater 2012;60:5160–71. https://doi.org/10.1016/j.actamat.2012.06.014.

[50] Hancock GG, Johnson HH. Hydrogen, oxygen and subcritical crack growth in a high-strength steel. Trans Metall Soc AIME 1966;236:513–6.

[51] Wan L, Geng WT, Ishii A, Du J-P, Mei Q, Ishikawa N, et al. Hydrogen embrittlement controlled by reaction of dislocation with grain boundary in alpha-iron. Int J Plast 2019;112:206–19.

[52] Matsumoto R, Taketomi S, Matsumoto S, Miyazaki N. Atomistic simulations of hydrogen embrittlement. Int J Hydrogen Energy 2009;34:9576–84. https://doi.org/10.1016/J.IJHYDENE.2009.09.052.

[53] Taketomi S, Matsumoto R, Miyazaki N. Atomistic simulation of the effects of hydrogen on the mobility of edge dislocation in alpha iron. J Mater Sci 2008;43:1166–9. https://doi.org/10.1007/s10853-007-2364-5.

[54] Song J, Curtin WA. Atomic mechanism and prediction of hydrogen embrittlement in iron. Nat Mater 2013;12:145–51.

[55] Mees MJ, Pourtois G, Neyts EC, Thijsse BJ, Stesmans A. Uniform-acceptance force-bias Monte Carlo method with time scale to study solid-state diffusion. Phys Rev B 2012;85:134301. https://doi.org/10.1103/PhysRevB.85.134301.

[56] Knuth DE. The art of computer programming: seminumerical algorithms. 3rd ed. Reading, Massachusetts: Addison Wesley Longman; 1997.

[57] Plimpton S. Fast Parallel Algorithms for Short-Range Molecular Dynamics for the United States Department of Energy under Contract DE.ACO4-76DPOO789. J Comput Phys 1995;117:1–19.

[58] Shinoda W, Shiga M, Mikami M. Rapid estimation of elastic constants by

molecular dynamics simulation under constant stress. Phys Rev B 2004;69:1341031.

[59] Parrinello M, Rahman A. Strain fluctuations and elastic constants. J Chem Phys 1982;76:2662–6.

[60] Wang Z, Shi X, Yang X-S, He W, Shi S-Q, Ma X. Atomistic simulation study of the deformation-induced martensitic transformation from α-Fe single crystal during the mode-I fracture. Submitt to J Mater Sci 2020.

[61] Mendelev MI, Han S, Srolovitz DJ, Ackland GJ, Sun DY, Asta M. Development of new interatomic potentials appropriate for crystalline and liquid iron. Philos Mag 2003;83:3977–94. https://doi.org/10.1080/14786430310001613264.

[62] Ramasubramaniam A, Itakura M, Carter EA. Interatomic potentials for hydrogen in alpha-iron based on density functional theory. Phys Rev B 2010;81:099902.

[63] Tsai DH. The virial theorem and stress calculation in molecular dynamics. J Chem Phys 1979;70:1375–82.

[64] Barber CB, Dobkin DP, Dobkin DP, Huhdanpaa H. The Quickhull Algorithm for Convex Hulls. ACM Trans Math Softw 1996;22:469–83. https://doi.org/10.1145/235815.235821.

[65] Rooke DP, Cartwright DJ. Compendium of stress intensity factors. London: Her Majesty's Stationery Office, The Hillingdon Press; 1976.

[66] Xie D, Qian Q, Li C. Numerical calculation methods and Engineering Application in fracture Mechanics (in Chinese). Beijing: Science Press; 2009.

[67] Irwin GR. Analysis of Stresses and Strains near the End of a Crack Traversing a Plate. J Appl Mech ASME 1957;E24:351–69.

[68] Jones E, Oliphant T, Peterson P, Others. SciPy: Open source scientific tools for Python 2001. http://www.scipy.org/.

[69] DasGupta A. Probability for Statistics and Machine Learning: Fundamentals and Advanced Topics. New York: Springer New York; 2011. https://doi.org/10.1007/978-1-4419-9634-3_1.

[70] Sean Gillies O. Shapely: manipulation and analysis of geometric objects 2017. https://github.com/Toblerity/Shapely.

[71] Oliphant T. NumPy: A guide to NumPy 2006. http://www.numpy.org/.

[72] Momma K, Izumi F. VESTA3 for three-dimensional visualization of crystal, volumetric and morphology data. J Appl Crystallogr 2011;44:1272–6. https://doi.org/10.1107/S0021889811038970.

[73] Stukowski A. Visualization and analysis of atomistic simulation data with OVITO -- The Open Visualization Tool. Model Simul Mater Sci Eng 2010;18:15012.

[74] Stukowski A, Bulatov V V, Arsenlis A. Automated identification and indexing of dislocations in crystal interfaces. Model Simul Mater Sci Eng 2012;20:85007. https://doi.org/10.1088/0965-0393/20/8/085007.

[75] Stukowski A. Structure identification methods for atomistic simulations of crystalline materials. Model Simul Mater Sci Eng 2012;20:45021. https://doi.org/10.1088/0965-0393/20/4/045021.

[76] Cleveland WS. Robust locally weighted regression and smoothing scatterplots. J Am Stat Assoc 1979;74:829–36. https://doi.org/10.1080/01621459.1979.10481038.

[77] Seabold S, Perktold J. Statsmodels: Econometric and Statistical Modeling with Python. PROC 9th PYTHON Sci CONF 2010:57.

[78] Ni XD, Wang Z, Sun X, Shen J, Chen NX. Mechanism of Ag and Al on improving the glass forming ability of CuZr-based alloys. Int J Miner Metall Mater 2011;18:424–9. https://doi.org/10.1007/s12613-011-0457-2.

[79] Fung YC. A first course in continuum mechanics. 2nd editio. Englewood Cliffs: Prentice-Hall, Inc.; 1977.

[80] Cottrell AH. Theory of brittle fracture in steel similar metals. Trans Metall Soc AIME 1958;212:192–203.

[81] Merkel S, Liermann H-P, Miyagi L, Wenk H-R. In situ radial X-ray diffraction study of texture and stress during phase transformations in bcc-, fcc- and hcp-iron up to 36 GPa and 1000 K. Acta Mater 2013;61:5144–51.

https://doi.org/10.1016/J.ACTAMAT.2013.04.068.

[82] Zhou XY, Yang XS, Zhu JH, Xing F. Atomistic simulation study of the grain-size effect on hydrogen embrittlement of nanograined Fe. Int J Hydrogen Energy 2020;45:3294–306. https://doi.org/10.1016/j.ijhydene.2019.11.131.

[83] Uyama H, Nakashima M, Morishige K, Mine Y, Murakami Y. Effects of hydrogen charge on microscopic fatigue behaviour of annealed carbon steels. Fatigue Fract Eng Mater Struct 2006;29:1066–74. https://doi.org/10.1111/j.1460-2695.2006.01069.x.

[84] Olson GB, Cohen M. A mechanism for the strain-induced nucleation of martensitic transformations. J Less Common Met 1972;28:107–18. https://doi.org/10.1016/0022-5088(72)90173-7.

[85] Olson GB, Cohen M. A general mechanism of martensitic nucleation: Part I. General concepts and the FCC → HCP transformation. Metall Trans A 1976;7:1897–904. https://doi.org/10.1007/BF02659822.

[86] Yang X-S, Sun S, Wu X-L, Ma E, Zhang T-Y. Dissecting the Mechanism of Martensitic Transformation via Atomic-Scale Observations. Sci Rep 2014;4:6141.

[87] Yang X-S, Sun S, Ruan H-H, Shi S-Q, Zhang T-Y. Shear and shuffling accomplishing polymorphic fcc γ → hcp ε → bct α martensitic phase transformation. Acta Mater 2017;136:347–54. https://doi.org/10.1016/J.ACTAMAT.2017.07.016.

[88] Dong Q, Zai S, Sun J, Liu M. Tensile Test Rate and Its Control in GB/T228.1-2010 Standard. Phys Test Chem Anal Part A(Physical Testing) 2011;47:774–81.

[89] Koh SJA, Lee HP, Lu C, Cheng QH. Molecular dynamics simulation of a solid platinum nanowire under uniaxial tensile strain: Temperature and strain-rate effects. Phys Rev B 2005;72:085414.

[90] Momotani Y, Shibata A, Terada D, Tsuji N. Effect of strain rate on hydrogen embrittlement in low-carbon martensitic steel. Int J Hydrogen Energy 2017;42:3371–9. https://doi.org/https://doi.org/10.1016/j.ijhydene.2016.09.188.

[91] Larson R, Farber B. Elementary Statistics : Picturing the World. 6th ed. New York, United States: Person; 2015.

[92] Spitzig WA, Keh AS. Orientation and temperature dependence of slip in iron single crystals. Metall Trans 1970;1:2751. https://doi.org/10.1007/BF03037811.

[93] Xing X, Yu M, Chen W, Zhang H. Atomistic simulation of hydrogen-assisted ductile-to-brittle transition in α-iron. Comput Mater Sci 2017;127:211–21. https://doi.org/10.1016/j.commatsci.2016.10.033.

[94] Allen MP, Tildesley DJ, Banavar JR. Computer Simulation of Liquids. New York,US: Oxford University Press; 1987.